RSC Advances

ROYAL SOCIETY OF CHEMISTRY

www.rsc.org/advances

One-Step Anion-Assisted Electrodeposition of ZnO Nanofibrous Networks as Photoanodes for Dye-Sensitized Solar Cells

İlkay Şişman,[a,*] Melike Can,[a] Bahar Ergezen,[a] and Mustafa Biçer,[b]

[a]*Department of Chemistry, Faculty of Arts and Sciences, Sakarya University, 54187, Sakarya, Turkey*

[b]*Department of Energy Systems Engineering, Faculty of Technology in Elbistan, Kahramanmaraş Sütçü İmam University, 46300, Kahramanmaraş, Turkey*

Tel: +90-264-2956063; Fax: +90-264-2955950; e-mail: isisman@sakarya.edu.tr

*Author to whom correspondence should be addressed.

Abstract

A highly efficient ZnO photoanode consisting of three-dimensional (3D) nanofibrous-like networks (NFs) for dye-sensitized solar cells (DSSCs) was synthesized by a one-step and seed-layer-free electrodeposition on a indium-tin-oxide (ITO) substrate at 75^{o}C in a solution containing $Zn(NO_3)_2$, KCl, $NaCH_3COO$, and $Na_3C_6H_5O_7$. In this solution, KCl as the supporting electrolyte promotes reduction of NO_3^- and diffusion of Zn^{2+} and CH_3COO^- and $C_6H_5O_7^{3-}$ anions as the capping agents selectively inhibit the ZnO growth along the c-axis. The photoelectrochemical results revealed that the DSSC based on ZnO NFs has the highest power conversion efficiency (3.78%) in comparison with those of the DSSCs based on nanosheets (1.36%), nanorods (2.18%), and microplates (2.55%). It can be attributed to the large dye adsorption amount, efficient light scattering and direct electron transfer networks, hence leading to a significant improvement of solar cell performance. Therefore, the ZnO NFs structure can be considered as a promising and efficient photanode for DSSCs.

Keywords: ZnO, nanofibrous networks, electrodeposition, photoanode, dye-sensitized solar cell

Introduction

Recently, ZnO-based nanomaterials, an important II-VI semiconductor with a wide band gap of 3.37 eV and a large exciton binding energy of 60 meV,[1] has attracted considerable interest due to their range of potential applications such as dye-sensitized solar cells (DSSCs),[2] light-emitting diodes,[3] sensors,[4] and nanogenerators.[5] In the early reports on ZnO-based DSSCs, ZnO nanoparticles were often used as the photoanode.[6] Photoexited electrons diffuse through the nanoparticles to the conductive substrate, via a series of interparticle hopping steps.[7] However, the excess electron hopping through the interparticle barriers could result in a long dwell time within individual particles and thus increase probability of charge recombination between the injected electrons and oxidized dye or redox electrolyte.[8] Recently, 1D ZnO nanomaterials, such as nanorods, and nanotubes, with direct electric pathways are particularly attractive as photoanodes of DSSCs due to their high electron mobility, increased electron diffusion length, which reduces the number of interparticle hops, and easy tailoring of the nanostructure via a mild wet-chemical method compared with conventional TiO_2.[9-11] However, the insufficient internal surface area of those 1D nanomaterials inhibits significant improvement of the photovoltaic efficiency due to their weak capability of dye loading and light harvesting.[9] To overcome these problems, multi-scale hierarchical structures were used as photoanode, including 3D nanofiber networks,[12] nanorods/nanosheets,[13] nanoforests,[14] nanowires/nanoparticles,[15] and microspheres/nanowires.[16] Among them, 3D nanofiber networks are particularly attractive as photoanodes due to their a high-conductivity network for efficient electron transport, a high roughness factor for dye loading, and large pores for enhanced light harvesting through light scattering.[17]

Several methods have been previously used for the preparation of ZnO nanofibers as photoanodes of DSSCs including electrospinning,[12] thermal evaporation,[18] and magnetron sputtering.[19] To our knowledge, however, there is no study on the

electrodeposition of ZnO nanofibers or fibrous-like nanostructures as photoanodes of DSSCs. Electrodeposition is a simple and effective method to synthesize the nanomaterials because of its economic nature, ease of scale-up, fine selectivity, ability to work at low temperatures, and environmental friendliness.[20-24]

In this paper, we report the one-step anion-assisted electrodeposition of 3D ZnO nanofibrous-like networks (NFs) in the presence of KCl, $NaCH_3COO$, and $Na_3C_6H_5O_7$. The deposition potential was fixed using the cyclic voltammetry experiments. The structural and morphological characteristics of the products are presented and discussed. The photovoltaic properties of the DSSC based on NFs photanode are discussed on the basis of incident photon-to-current efficiency (IPCE), photocurrent-voltage (*J-V*), and electrochemical impedance spectroscopy (EIS) and compared to other the DSSCs based on ZnO multi-scale structures, such as nanorods, nanosheets and microplates. An enhanced conversion efficiency of the DSSC based on NFs was 3.78%, which were largely improved compared with those of the other DSSCs.

Experimental

Materials Synthesis

The electrodeposition of the ZnO samples and cyclic voltammetry studies were was performed in an electrochemical cell immersed in a water bath held at 75^{o}C by a PARSTAT 2273 model potentiostat/galvanostat (Princeton Applied Research). The electrochemical cell consisted of an indium-tin-oxide (ITO, 8-12 Ωcm^{-2}) coated glass working electrode, a zinc plate counter electrode,[25] and an Ag/AgCl reference electrode (Bioanalytical Systems). All of the solutions used in this study were prepared with deionized water (resistivity $\geq$ 18 MΩcm). Prior to each experiment, the solutions were purged with purified N_2 gas. The solutions were moderately stirred by magnetic stirrer during both the electrodeposition and cyclic voltammetry studies. The deposition of the

ZnO samples was performed in a solution containing of 15 mM $Zn(NO_3)_2.4H_2O$ (Merck), and varying concentration of KCl (Merck), $NaCH_3COO$ (Merck), and $Na_3C_6H_5O_7.2H_2O$ (Merck) at ~ pH 6.0. All of the samples were synthesized at a constant potential of -0.950 V. In order to obtain nearly the same thickness of samples, the samples were deposited different deposition times from solutions 1-4 (Table 1). After deposition, the samples coated ITO substrates were thoroughly rinsed with deionized water and dried under a N_2 gas stream. Finally the samples were annealed at 350^{o}C for 30 min through a rapid annealing process prior to their assembly. The active areas of the photanodes were 0.16 cm^2 by scraping off the excess area.

Assembly of DSSCs

The resulting ZnO samples were sensitized by immersing them in 0.3 mM N719 (Ruthenizer 535-bisTBA, Solaronix) dye in acetonitrile/*tert*-butyl alcohol (v/v = 1:1) solution for 30 min at room temperature and then rinsed with absolute ethanol to remove the excess dye and dried in air. The counter electrode was prepared by spreading a H_2PtCl_6 solution (Platisol T, Solaronix) on the FTO (Fluorine-doped tin oxide, 13 Ωcm^{-2}) coated glass substrate and heating at 450^{o}C for 15 min. The counter electrode was then placed directly on the top of the dye-sensitized ZnO sealed with polymer foil (Meltonix 1170-25, Solaronix) as a spacer frame, then thermally treated at 100^{o}C for 5 min to bond the two electrodes. The I^-/I_3^- electrolyte (Iodolyte AN-50, Solaronix) was injected from one of two predrilled holes on the counter electrode into the space between the sandwiched cells. Then the holes were sealed by parafilm at elevated temperature.

Characterization

The prepared samples were subjected to SEM analysis in a JEOL JSM-6060LV to investigate the surface morphology. The XRD patterns for the samples were recorded

by Rigaku Advance Powder X-ray diffractometer (λ = 1.54050 Å) in the span of angle between 20° and 70°. The average thickness of the samples was measured by using a profiler (KLA Tencor P6). The amount of dye loaded into the samples was determined by desorbing the dye from the sample surface (1 x 2 cm^2) into a 0.1 M NaOH aqueous solution and measuring its absorption spectrum by a UV-vis spectrophotometer (UV-2401, Shimadzu). The diffused reflectance spectra of the ZnO samples were measured using a UV−vis spectrophotometer (UV-2600, Shimadzu). The *J-V* curves of DSSCs were recorded by above-mentioned potentiostat/galvanostat under illumination of simulated sunlight (100 mW cm^{-2}) provided by a solar simulator (Model 96000, Newport) with an AM 1.5G filter. A 150 W xenon lamp (Oriel) used as the light source. The incident light intensity was calibrated using a standard Si detector (Model 918D-SL-OD3, Newport) and an optical power meter (Model 1917-R, Newport). The fill factor (*FF*) and the power conversion efficiency (η) of DSSCs were calculated according to the following equations.[26]

$$FF = \frac{V_{max} \times J_{max}}{V_{oc} \times J_{sc}} \quad (1)$$

$$\eta\% = \frac{V_{max} \times J_{max}}{P_{in}} \times 100 = \frac{V_{oc} \times J_{sc} \times FF}{P_{in}} \times 100 \quad (2)$$

J_{sc} is the short-circuit current density (mA cm^{-2}), V_{oc} is the open-circuit voltage (*V*), P_{in} is the incident light intensity (mW cm^{-2}) and J_{max} (mA cm^{-2}) and V_{max} (*V*) are the current density and voltage at the point of maximum power output in the *J-V* curves, respectively. The electrochemical impedance spectroscopy (EIS) measurements of the DSSCs were performed by the potentiostat/galvanostat and carried out by applying bias of the open-circuit voltage (V_{oc}) under a constant light illumination of 100 mW cm^{-2} and recorded over a frequency range of 10^{-1} to 10^5 Hz with AC amplitude of 10 mV. The incident photon-to-current efficiency (IPCE) curves of the DSSCs were obtained by

using the potentiostat/galvanostat and solar simulator equipped with a monochromator (Model 74004, Oriel). The IPCE was calculated using the following equation.[27]

$$IPCE(\lambda)\ (\%) = 1240 \times \left(\frac{J_{sc}}{\lambda \times P_{in}}\right) \times 100 \quad (3)$$

J_{sc} is the short-circuit current density (mA cm^{-2}), λ is the monochromatic incident light wavelength (nm) and P_{in} is the incident light intensity at that wavelength (mW cm^{-2}).

Result and Discussion

Cyclic voltammetry

In order to determine the electrodeposition potential, cyclic voltammetry experiments were performed on the ITO substrates. The cyclic voltammogram (CV) for the solution containing only 15 mM $Zn(NO_3)_2$ is shown in Fig. 1a. The relatively broad cathodic peak is observed between -0.500 to -1.250 V where the ZnO electrodeposition is expected by the following reactions.[28]

$$Zn(NO_3)_2 \leftrightarrow Zn^{2+} + 2NO_3^- \quad (4)$$

$$NO_3^- + H_2O + 2e^- \rightarrow NO_2^- + 2OH^- \quad (5)$$

$$Zn^{2+} + 2OH^- \rightarrow Zn(OH)_2 \quad (6)$$

$$Zn(OH)_2 \rightarrow ZnO + H_2O \quad (7)$$

The steep peak observed from -1.250 to -1.500 V could be due to the metallic deposition of Zn and H_2 evolution reaction. In the reverse scan, the anodic current is negligible indicating the high stability of the deposited ZnO.[29] The CV for the solution containing mixture of 15 mM $Zn(NO_3)_2$ and 0.1 M KCl is shown in Fig. 1b. It can be seen that the reduction of NO_3^- and onset of metallic Zn deposition slightly shift to more positive potentials as compared with that of the solution of $Zn(NO_3)_2$. This could be due

to that the KCl resulted in the increase in electrolyte conductivity and accelerating the diffusions of Zn^{2+} and reduction of NO_3^-.[30] Furthermore, in contrast to the behavior observed for the solution of $Zn(NO_3)_2$, an anodic peak appeared at around -0.700 V in the reverse scan. Similar anodic peaks were observed for the solutions containing 15 mM $Zn(NO_3)_2$ + 1 mM $Na_3C_6H_5O_7$ and 15 mM $Zn(NO_3)_2$ + 1 mM $NaCH_3COO$ in Fig. 1c and d, respectively. These anodic peaks seem to result from the oxidation of adsorbed of Cl^-, CH_3COO^- and $C_6H_5O_7^{3-}$ anions on the ZnO surface. The oxidation processes may be represented as:[31-33]

$$Cl^- \rightarrow Cl + e^- \quad (8)$$

$$CH_3COO^- \rightarrow CH_3COO + e^- \quad (9)$$

$$C_6H_8O_7 \leftrightarrow C_6H_5O_7^{3-} + 3H^+ \quad (10)$$

In the last process, the subsequent step involves the oxidation of the adsorbed $C_6H_5O_7^{3-}$ ion.[33] Based on the above results, if the deposition is carried out in the solution containing 15 mM $Zn(NO_3)_2$ + 0.1 M KCl + 1 mM $NaCH_3COO$ + 1 mM $Na_3C_6H_5O_7$ at potential range of -0.400 to -1.05 V, ZnO will be formed at the ITO surface. For the Cl^- adsorption, the CVs were also performed in the lower concentrations than 0.1 M KCl but a noticeable anodic peak was not observed (not shown here). When the concentrations of the anions were considered, the Cl^- anion showed the lowest adsorption on the ZnO. Pradhan and Leung carried out a study on the electrodeposition of ZnO films in presence of KCl solutions.[34] They inferred that the slow hydroxylation reaction (eq 6) allows sufficient time for ion exchange, hence hindering significant surface capping by Cl^- anions in the solution containing mixture of 0.1 M KCl and 10 mM $Zn(NO_3)_2$. However, at a sufficiently high concentration of KCl (>0.1 M), the capping effect of Cl^- will occur.

Morphological and structural characterization

The influence of KCl on the morphology of the deposited ZnO samples was investigated. Fig. 2a and b show the SEM image of the ZnO samples deposited at -0.950 V for 3 h in the absence and presence of 0.1 M KCl (solution 1), respectively. In the $Zn(NO_3)_2$ solution with KCl, the nanorod arrays (NRs) along the c-axis direction and hexagonal planes are obtained whereas the spike-like nanorods are observed the solution containing only $Zn(NO_3)_2$. This obviously confirms the role of Cl^- adsorption on the positive polar (0001) crystal plane, causing the formation of hexagon on the top of ZnO nanorods. However, an apparent change in the morphology of samples is not found in Fig. 2a and b, revealing that Cl^- has not an effect on the growth along c-axis when the concentration of Cl^- is 0.1 M. The weak adsorption of Cl^- on ZnO is in agreement with the literature.[34] However, it was found that the thickness of the deposited ZnO sample (2.6 μm) in the absence of KCl was thinner than that of the deposited in the presence of KCl (Table 1). This may be due to that the KCl resulted in the increase in solution conductivity and accelerating the diffusions of Zn^{2+} and reduction of NO_3^-. Thus, it was decided that the solution with KCl (solution 1) would be more appropriate for deposition of nanorods.

In order to define the effect of CH_3COO^- and $C_6H_5O_7^{3-}$ on the shape and size of the ZnO samples, depositions were performed from solutions 2 and 3, respectively (Fig. 1c and d). In the solution with CH_3COO^-, the porous vertically aligned microplate-like structures consist of nanoparticles (MPs) are obtained whereas the nanosheet-like networks (NSs) are observed the solution containing CH_3COO^- and $C_6H_5O_7^{3-}$. Similar structures have been observed for the electrodeposition of ZnO in the presence of CH_3COO^- or $C_6H_5O_7^{3-}$.[35,36] This clearly confirms the strong adsorption of CH_3COO^- and $C_6H_5O_7^{3-}$ on the (0001) plane, causing the formation of plate or sheet structures. The strong adsorption behavior is also verified by CV results. On the other hand, a clear difference in the morphology of samples is found in Fig. 2c and d. The difference may

be related to the adsorption mechanism of $C_6H_5O_7^{3-}$, which can form complex $[Zn(C_6H_5O_7)_4]^{10-}$ with Zn^{2+}.[36] Thus, this complex is preferred to (0001) plane and decrease the growth rate of (0001) plane or the corresponding (002) peak, which leads to the formation of ZnO NSs with the contribution of CH_3COO^-.

The SEM images with different magnifications of the ZnO sample obtained from the solution containing KCl, CH_3COO^- and $C_6H_5O_7^{3-}$ (solution 4) are shown in Fig. 2e, f and S1. It can be clearly seen that the morphology evolves from nanosheet networks to 3D dense porous nanofibrous-like networks (NFs). These results indicate that the less conducting electrolytes give rise to less densely nanosheets, while more conducting electrolytes produce more densely nanofibrous-like networks. Briefly, the highly conducting media enhance the diffusion of Zn^{2+} and reduction of NO_3^-, resulting in dense nanofibrous-like networks growth. The effect of electrolyte on the ZnO is in agreement with what has been reported previously.[30,37]

Fig. 3 shows the corresponding XRD patterns of ZnO NRs, MPs, NSs, and NFs deposited on ITO substrates from solutions 1-4, respectively. All the presented diffraction peaks, except for those of ITO, can be indexed to hegzagonal wurtzite ZnO structure (JCPDS 01-089-0511). It can be seen that the peak intensities vary with the morphhology of the ZnO samples. For ZnO NRs, the relative intensity of the (002) peak is increased significantly, with the (100) and (101) peak intensities reduced, which is as expected from their c-axis growth. However, in Fig. 3 b-d, the relative intensity of the (002) peaks is found to be drastically decreased, suggesting the transformation from NRs to NFs, as shown in Fig. 2. This revealed that the CH_3COO^- and $C_6H_5O_7^{3-}$ ions adsorb on positive polar (0001) plane and suppressed ZnO growth along c-axis or the intensity of corresponding (002) peak. The resulting NFs therefore have the preferred growth direction of (100) peak or nonpolar $(10\bar{1}0)$ plane. The similar results have been reported for ZnO nanostructures.[34,38]

Performance of DSSCs

To determine the effect of the morphologies of the ZnO samples on the performances of the DSSCs, we fabricated cells with NRs, MPs, NSs and NFs as photoanodes. Fig. 4 compares the typical $J-V$ curves of DSSCs based on the photanodes and the corresponding photoelectrochemical parameters are listed in Table 2. For all the samples, the V_{oc} of ca. 0.55 V, indicating that there was no significant effect of morphology on V_{oc} of DSSCs in this study. This was attributed that the V_{oc} was proportional to the energy difference between the semiconductor Fermi level and the redox potential of the electrolyte.[39] However, the value of the J_{sc} is increased from 8.12 to 14.42 mA cm^{-2} with the morphology of photoanode changed from the NSs to the NFs. Consequently, the power conversion efficiency remarkably improves from 1.36% to 3.78%.

The IPCE curves would more detail information the photoelectrochemical performance of the ZnO samples are shown in Fig. 5. The maximum IPCE values of the four samples with N719 dye occur at approximately 520 nm. The integrated IPCE values are all in good agreement with the measured J_{sc} shown in Fig. 4. Compared with the other samples, the ZnO NFs has a higher IPCE from 400 to 750 nm wavelength ranges. The enhanced IPCE for the NFs in the shorter wavelengths (400-600 nm) can be attributed to high dye adsorption while the improved IPCE in the longer wavelengths (600-750 nm) can be ascribed to the efficient light scattering. As a result, the highest IPCE value of the DSSC based on NFs can indicate maximized use of solar light, which further enhances the light harvesting efficiency and improves the J_{sc}.[40]

In order to verify high dye adsorption, the amount of adsorbed dye on the ZnO samples were calculated from the UV-vis spectra using the Lambert–Beer's law as follows (Fig. 6 and Table 2):

$$A = \varepsilon lc \quad (11)$$

where A is the absorbance of the UV-vis spectra at 515 nm, ε = 14100 M^{-1} cm^{-1} is the molar extinction coefficient of the dye at 515 nm, l is the path length of the light beam, and c is the dye concentration.[41] As expected, the NFs sample shows the highest dye adsorption due to its relatively specific area, which is in well agreement with the IPCE results.

To further understand light scattering ability, the diffused reflectance spectra of ZnO samples with different morphologies were measured (Fig. 7). The reflectance spectrum of the NFs was about 68% in the range of 300−800 nm, which was higher than the other samples, indicating that the incident light was efficiently scattered within NFs, which would lead to a higher photocurrent in DSSC based on NFs. The higher light scattering ability might be caused by repeated light reflection in the 3D porous structure.

To better understand the effects of morphology on the electron transfer properties of DSSCs, EIS was used, and the Nyquist and Bode plots are shown in Fig. 8a and b, respectively. The internal impedances were determined by fitting the experimental data with an equivalent circuit (inset of Fig. 8a). As is shown, there are two semicircles on the Nyquist plots, of which the one in the low frequency region shows a bigger radius than the other one in the higher frequency region. The large semicircles are assigned to the charge transfer process occurring at the ZnO/dye/electrolyte interface (R_2) and the small semicircles correspond to the resistance of the Pt/redox (I^-/I_3^-) interface charge transfer (R_1). *Rs* is the series resistance, including the sheet resistance of the ITO glass and the contact resistance of the cell, whose semicircle cannot be seen actually.[42] It can be seen that the second semicircle of the DSSC based on NFs is smaller than that of the DSSCs based on other samples. That is

to say, the resistance of electron transfer (R_2) is lowest in the DSSC based on NFs (Table 2). The smaller electron transfer impedance implies the faster electron transfer, which can hinder the electron recombination and results in higher photocurrent and efficiency. This is mainly originating from the direct electron transfer pathway and the tight connection of fibrous-like structures in the ZnO NFs.

This result is also supported by the corresponding Bode plots (Fig. 8b), which displays the characteristic frequency peaks of charge transfer process for DSSCs. Based on the maximum frequency (f_{max}) of the peak at intermediate frequency, the electron lifetime (τ_e) for these four DSSCs can be calculated using to the following formula.[43]

$$\tau_e = \frac{1}{2\pi f_{max}} \quad (12)$$

As can be seen from Table 2, the DSSC based on NFs shows the longest electron lifetime among those DSSCs tested. Therefore, the enhanced electron lifetime suggests that the photogenerated electrons can diffuse farther without interruption.[44] Consequently, the lower resistance and the longer electron lifetime could favor a higher charge collection rate of produced electrons, which improves the efficiency of DSSC.

Conclusions

In summary, we have developed a one-step anion-assisted electrodeposition method for fabricating 3D ZnO nanofibrous-like networks as photoanodes for DSSCs. Detailed morphological and structural investigations show that the addition of KCl, $NaCH_3COO$ and $Na_3C_6H_5O_7$ play a key role in driving the growth of the nanofibrous-like networks. Compared with the micro plates, nanorods and nanosheets, the 3D nanofibrous-like networks show the highest efficiency of 3.78%, with a high J_{sc} of 14.4 mA cm^{-2}, a FF of 0.46, a τ_e of 8.2 ms and low a R_2 of 16.3 Ω, which can be mainly ascribed to higher charge transfer rate, sufficient dye adsorption and better light

scattering capacity. The simple method for the fabrication of the ZnO nanofibrous-like networks is promising for the development of the low-cost and ecofriendly devices with high power conversion efficiency.

Acknowledgements

The authors are grateful for financial support provided by the Commission of Science Research of Sakarya University (No. 2014-50-01-011).

References

1 M. H. Huang, S. Mao, H. Feick, H. Q. Yan, Y. Y. Wu, H. Kind, E. Weber, R. Russo and P. D. Yang, *Science*, 2001, **292**, 1897-1899.

2 S. B. Zhu, L. M. Shan, X. N. Chen, L. He, J. J. Chen, M. Jiang, X. L. Xie and Z. W. Zhou, *RSC Adv.*, 2013, **3**, 2910-2916.

3 J. M. Bao, M. A. Zimmler, F. Capasso, X. W. Wang and Z. F. Ren, *Nano Lett.*, 2006, **6**, 1719-1722.

4 C. W. Na, H. S. Woo and J. H. Lee, *RSC Adv.*, 2012, **2**, 414-417.

5 Z. L. Wang and J. Song, *Science*, 2006, **312**, 242-246.

6 K. Keis, E. Magnusson, H. Lindstrom, S. E. Lindquist and A. Hagfeldt, *Sol. Energ. Mater. Sol. Cell.*, 2002, **73**, 51-58.

7 J. B. Baxter, A. M. Walker, K. van Ommering and E. S. Aydil, *Nanotechnology*, 2006, **17**, S304-S312.

8 F. Xu, M. Dai, Y. N. Lu and L. T. Sun, *J. Phys. Chem. C*, 2010, **114**, 2776-2782.

9 M. Law, L. E. Greene, J. C. Johnson, R. Saykally and P. D. Yang, *Nat. Mater.*, 2005, **4**, 455-459.

10 Q. F. Zhang, C. S. Dandeneau, X. Y. Zhou, and G. Z. Cao, *Adv. Mater.*, 2009, **21**, 4087-4108.

11 A. I. Hochbaum and P. D. Yang, *Chem. Rev.*, 2010, **110**, 527-546.

12 I. D. Kim, J. M. Hong, B. H. Lee, D. Y. Kim, E. K. Jeon, D. K. Choi and D. J. Yang, *Appl. Phys. Lett.*, 2007, **91**, 163109.

13 J. H. Qiu, M. Guo and X. D. Wang, *ACS Appl. Mater. Inter.*, 2011, **5**, 2358-2367.

14 S. H. Ko, D. Lee, H. W. Kang, K. H. Nam, J. Y. Yeo, S. J. Hong, C. P. Grigoropoulos and H. J. Sung, *Nano Lett.*, 2011, **11**, 666-671.

15 L. Y. Chen and Y. T. Yin, *RSC Adv.*, 2013, **3**, 8480-8488.

16 X. H. Kang, C. Y. Jia, Z. Q. Wan, J. Zhuang and J. Feng, *RSC Adv.*, 2015, **5**, 16678-16683.

17 N. Tetreault, E. Horvath, T. Moehl, J. Brillet, R. Smajda, S. Bungener, N. Cai, P. Wang, S. M. Zakeeruddin, L. Forro, A. Magrez, and M. Gratzel, *ACS Nano*, 2010, **4**, 7644-7650.

18 S. Li, X. Z. Zhang, X. J. Jiao and H. Lin, *Mater. Lett.*, **65**, 2975-2978 (2011).

19 O. Lupan, V. M. Guerin, L. Ghimpu, I. M. Tiginyanu and T. Pauporte, *Chem. Phys. Lett.*, 2012, **550**, 125-129.

20 G. H. A. Therese and P. V. Kamath, *Chem. Mater.*, 2000, **12**, 1195-1204.

21 M. Biçer, H. Köse and İ. Şişman, *J. Phys. Chem. C*, 2010, **114**, 8256-8263.

22 İ. Şişman and H. Öz, *Electrochim. Acta*, 2011, **56**, 4889-4894.

23 M. Biçer and İ. Şişman, *Langmuir*, 2012, **28**, 15736-15742

24 M. Arpacık, M. Biçer and İ. Şişman, *J. Electrochem. Soc.*, 2013, **160**, A2250-A2257

25 M. Zi, M. Zhu, L. Chen, H. M. Wei, X. P. Yang and B. Q. Cao, *Ceram. Int.*, 2014, **40**, 7965-7970.

26 G. T. Yue, F. R. Tan, F. M. Li, C. Chen, W. F. Zhang, J. H. Wu and Q. H. Li, *Electrochim. Acta*, 2014, **149**, 117-125.

27 Y. G. Lin, Y. K. Hsu, Y. C. Chen, S. B. Wang, J. T. Miller, L. C. Chen and K. H. Chen, *Energy Environ. Sci.*, 2012, **5**, 8917-8922.

28 J. S. Wellings, N. B. Chaure, S. N. Heavens and I. M. Dhannadasa, *Thin Solid Films*, 2008, **516**, 3893-3898.

29 T. Mahalingam, V. S. John, M. Raja, Y. K. Su and P. J. Sebastian, *Sol. Energ. Mater. Sol. Cell.*, 2005, **88**, 227-235.

30 S. J. Jiao, K. J. Zhang, S. S. Bai, H. L. Li, S. Y. Gao, H. T. Li, J. Z. Wang, Q. J. Yu, F. Y. Guo and L. C. Zhao, *Electrochim. Acta*, 2013, **111**, 64-70.

31 J. Elias, R. Tena-Zaera and C. Levy-Clement, *J. Phys. Chem. C*, 2008, **112**, 5736-5741.

32 T. Fukuda and A. Aramata, *J. Electroanal. Chem.*, 1999, **467**, 112-120.

33 O. I. Gonzalez-Pena, T. W. Chapman, Y. M. Vong, and R. Antano-Lopez, *Electrochim. Acta*, 2008, **53**, 5549-5554.

34 D. Pradhan and K. T. Leung, *Langmuir*, 2008, **24**, 9707-9716.

35 C. W. Kung, H. W. Chen, C. Y. Lin, Y. H. Lai, R. Vittal, and K. C. Ho, *Prog. Photovoltaics*, 2014, **22**, 440-451.

36 L. Ding, R. X. Zhang and L. Z. Fan, *Nanoscale Res. Lett.*, 2013, **8**, 78.

37 M. Abd-Ellah, N. Moghimi, L. Zhang, N. F. Heinig, L. Y. Zhao, J. P. Thomas, and K. T. Leung, *J. Phys. Chem. C*, 2013, **117**, 6794-6799.

38 X. Bai, L. Yi, D. L. Liu, E. Y. Nie, C. L. Sun, H. H. Feng, J. J. Xu, Y. Jin, Z. F. Jiao and X. S. Sun, *Appl. Surf. Sci.*, 2011, **257**, 10317-10321.

39 X. J. Feng, K. Shankar, M. Paulose and C. A. Grimes, *Angew. Chem. Int. Edit.*, 2009, **48**, 8095-8098.

40 J. Y. Liao, J. W. He, H. Y. Xu, D. B. Kuang and C. Y. Su, *J. Mater. Chem.*, 2012, **22**, 7910-7918.

41 J. Zhi, A. Chen, H. L. Cui, Y. Xie and F. Q. Huang, *Phys. Chem. Chem. Phys.*, 2015, **17**, 5103-5108.

42 J. Liu, A. X. Wei, Y. Zhao, K. B. Lin and F. Z. Luo, *J. Mater. Sci.: Mater. Electron.*, 2014, **25**, 1122-1126.

43 K. S. Kim, H. Song, S. H. Nam, S. M. Kim, H. Jeong, W. B. Kim and G. Y. Jung, *Adv. Mater.*, 2012, **24**, 792-798.

44 K. Mahmood, H. W. Kang, S. B. Park and H. J. Sung, *ACS Appl. Mater. Inter.*, 2013, **5**, 3075-3084.

Tables

Table 1. Experimental conditions and thickness of ZnO samples

Solution	Composition of solutions (mM)				Deposition Time (h)	Thickness (μm)
	$Zn(NO_3)_2$	KCl	CH_3COO^-	$C_6H_5O_7^{3-}$		
1	15	100	-	-	3.0	3.2
2	15	-	1	-	3.5	3.0
3	15	-	-	1	3.5	2.9
4	15	100	1	1	3.0	3.1

Table 2. The photoelectrochemical parameters of DSSCs with different ZnO samples

Samples	Adsorbed dye (nmol cm^{-2})	J_{sc} (mA cm^{-2})	V_{oc} (V)	*FF*	η (%)	R_2 (Ω)	τ_e (ms)
NRs	48.9	10.7	0.55	0.37	2.18	35.4	4.7
MPs	61.0	11.9	0.55	0.39	2.55	27.4	6.6
NSs	37.5	8.1	0.54	0.31	1.36	41.6	3.3
NFs	80.2	14.4	0.57	0.46	3.78	16.3	8.2

Figure Captions

Figure 1. Cyclic voltammograms of 15 mM $Zn(NO_3)_2$ (a), 15 mM $Zn(NO_3)_2$ + 0.1 M KCl (b), 15 mM $Zn(NO_3)_2$ + 1 mM $Na_3C_6H_5O_7$ (c), and 15 mM $Zn(NO_3)_2$ + 1 mM $NaCH_3COO$ (d).

Figure 2. SEM images of ZnO nanorods (a, b), micro plates (c), nanosheets (d), and nanofibrous-like networks (e, f).

Figure 3. XRD patterns of NRs, MPs, NSs, and NFs.

Figure 4. $J-V$ curves of DSSCs based on NFs, NSs, MPs, and NRs.

Figure 5. IPCE curves of DSSCs with NFs, NSs, MPs, and NRs.

Figure 6. Optical absorption spectra of the solutions containing N719 desorbed from the sensitized ZnO photoanodes composed of different structures.

Figure 7. Diffused reflectance spectra of the different ZnO structures.

Figure 8. Nyquist (a) and Bode plots (b) of the DSSCs based on NSs, NRs, MPs, and NFs.

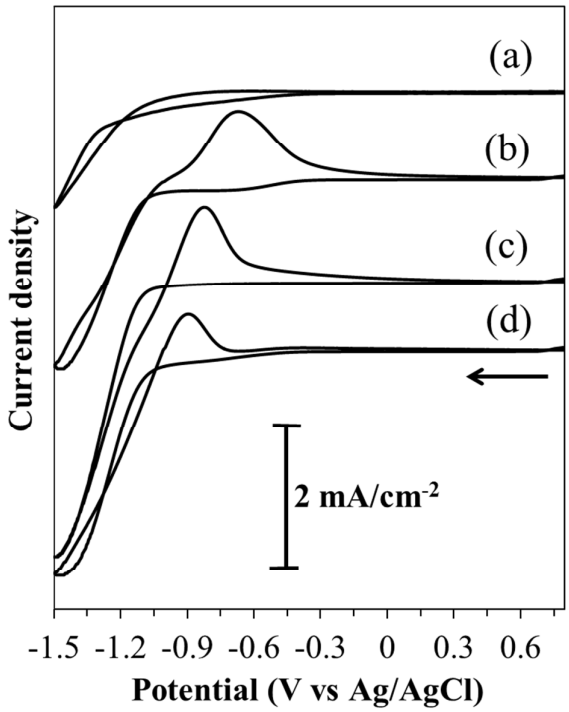

Figure 1.

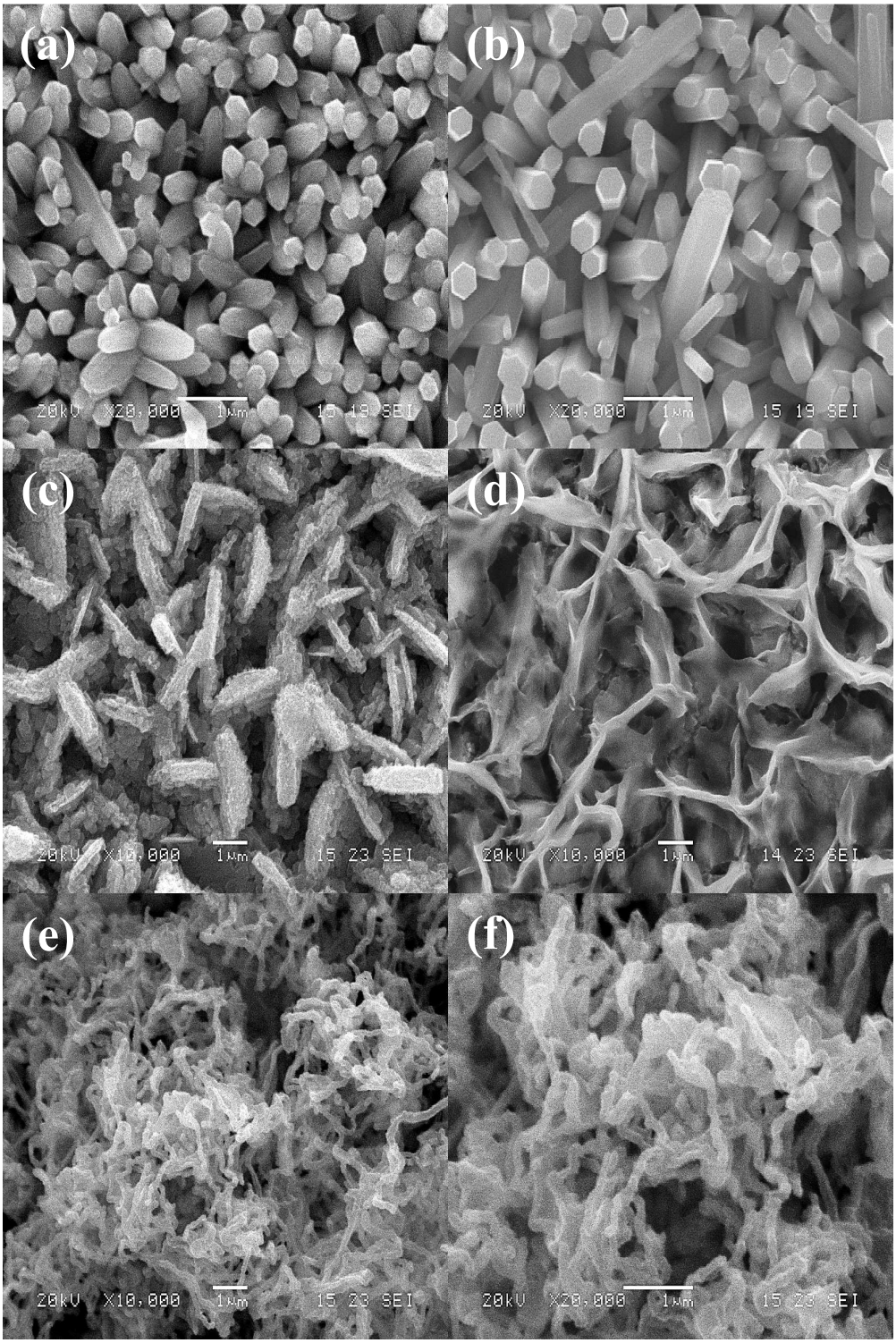

Figure 2.

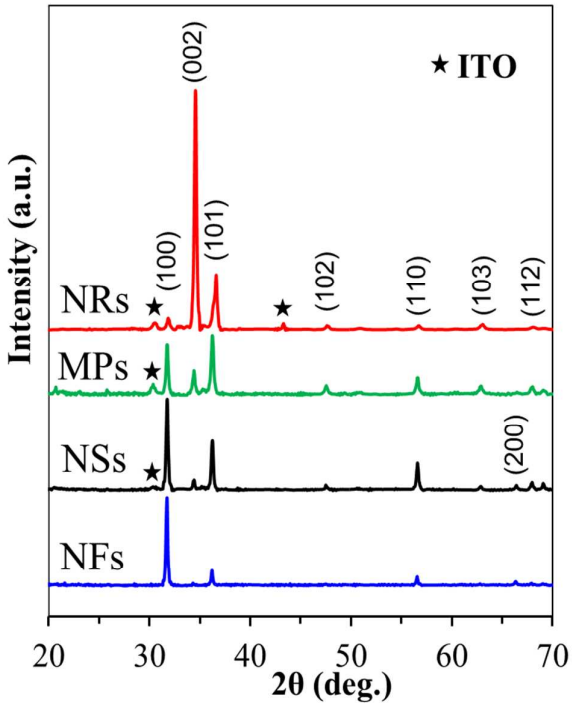

Figure 3.

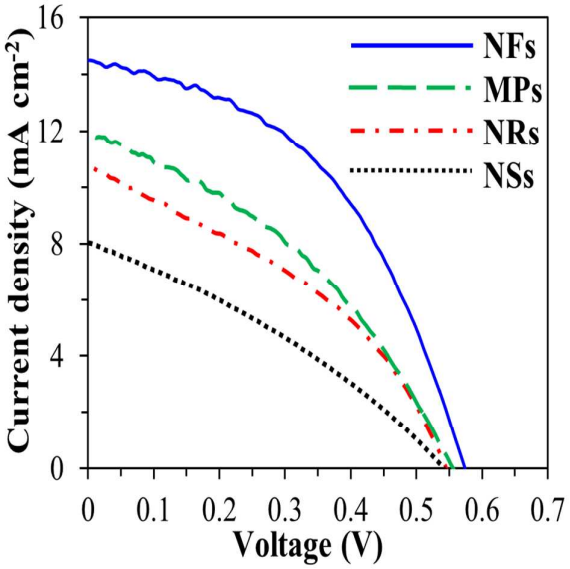

Figure 4.

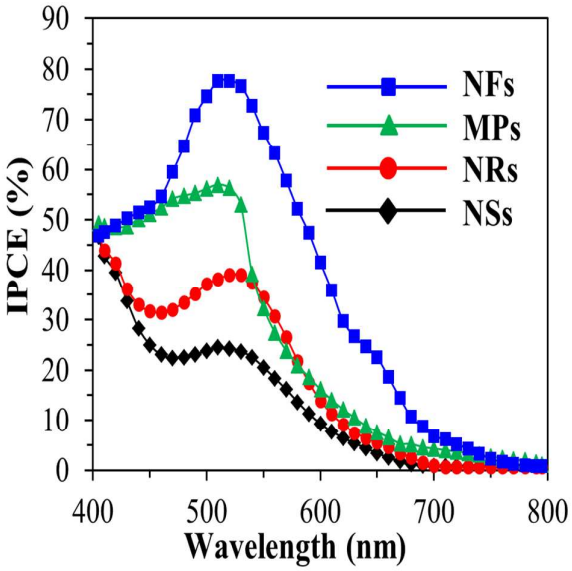

Figure 5.

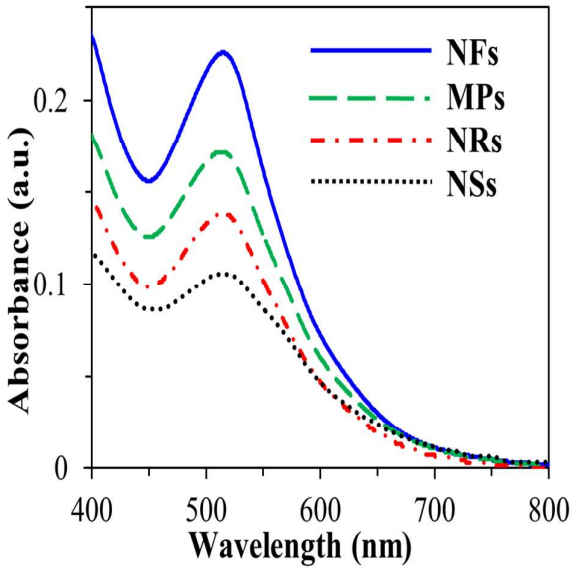

Figure 6.

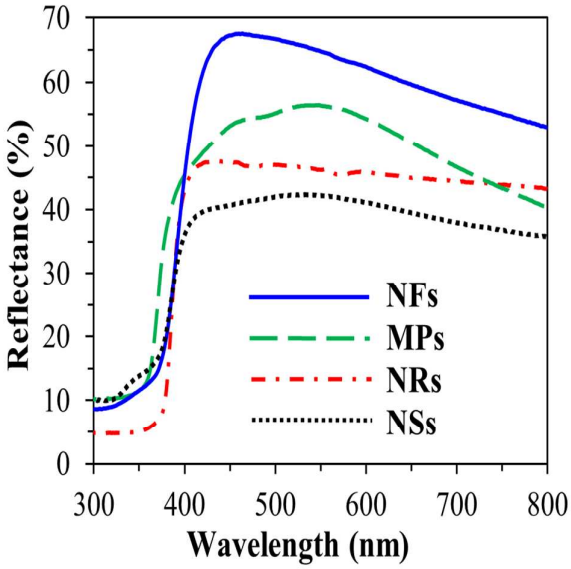

Figure 7.

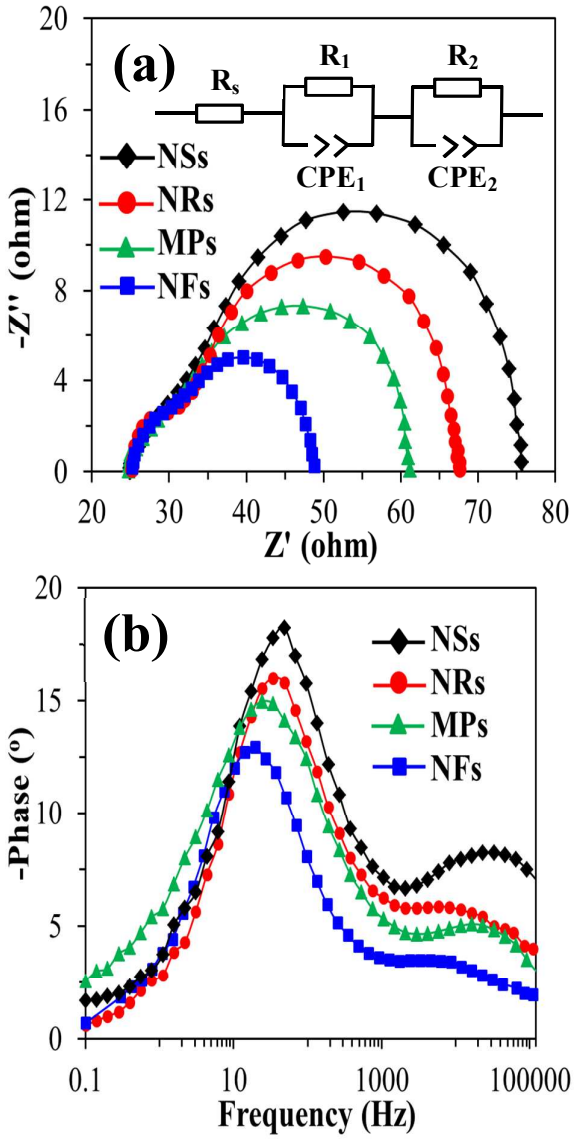

Figure 8.

Graphical abstract

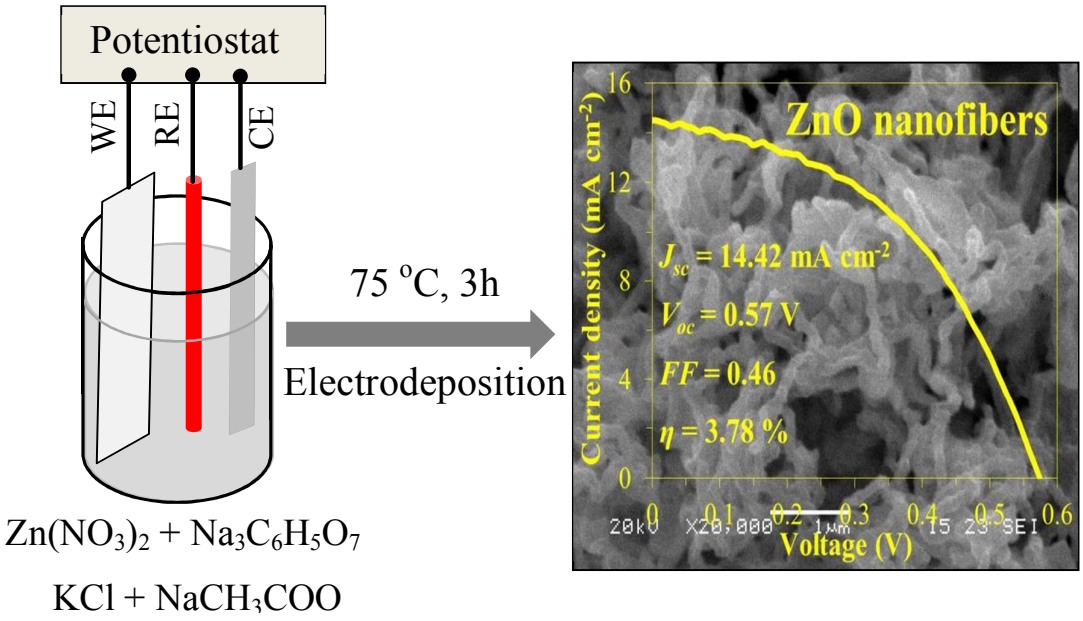

$Zn(NO_3)_2 + Na_3C_6H_5O_7$

$KCl + NaCH_3COO$